Tin re-deposition and erosion measured by Cavity-Ring-Down-Spectroscopy under a high flux plasma beam

V Kvon[1,2], R Al[2], K Bystrov[2], F J J Peeters[2], M C M van de Sanden[2] and T W Morgan[2]

[1]Department of Applied Physics, Ghent University, St Pietersnieuwstraat 41 B4, B-9000 Ghent, Belgium
[2]DIFFER - Dutch Institute for Fundamental Energy Research, De Zaale 20, 5612 AJ Eindhoven, The Netherlands

v.kvon@differ.nl

Abstract. Cavity-Ring-Down Spectroscopy (CRDS) was implemented to measure the re-deposition of liquid tin under a high flux plasma beam in the linear plasma device Pilot-PSI. A capillary porous system (CPS) consisting of a molybdenum cup and tungsten meshes (pores diameters of 0.2 mm and 0.44 mm) was filled with tin and exposed to argon plasma. The absorption of a UV laser-beam at 286.331 nm was used to determine a number of sputtered neutral tin atoms. The incoming flux of argon ions of ~50 eV was $1.6–2.7 \times 10^{23}$ $m^{-2}s^{-1}$, and the sample temperature measured by pyrometry varied from 850 °C to 1200 °C during exposures. The use of CRDS for measuring absolute number of particles under such plasma exposure was demonstrated for the first time. The number of sputtered tin particles in the cavity region assuming no losses would be expected to be $5.5 \times 10^{11}–1.2 \times 10^{12}$ while CRDS measurements showed only $5.7–9.9 \times 10^{8}$. About 98−99.8% of sputtered particles were therefore found to not reach the CRDS observation volume. Spectroscopic ratios of Sn I to Sn II ions, as well as equilibrium considerations, indicate that fast ionization as well as plasma entrainment of neutrals is responsible for the discrepancy. This would lead to high re-deposition rates, implying a lowered contamination rate of core plasma and lower required replenishment rates at high-flux conditions than would otherwise be expected.

Keywords: *tin erosion, CRDS, fusion, UV, liquid metals.*

1. Introduction

While tungsten will be used as the plasma facing material (PFM) for the divertor region in ITER [1], the duty cycle and particle fluence in the divertor of a fusion power-plant (i.e. DEMO) will exceed those in ITER considerably [2,3,4]. Furthermore neutron damage will degrade the material properties significantly over time [4, 5,6]. Uncontrolled Edge Localized Modes (ELMs) or disruptions would also lead to irreversible damage to the solid surface of any divertor plasma facing component (PFC). Therefore the choice of a suitable PFM remains challenging. The alternative principle of a liquid PFM is therefore studied in the current work.

Liquid metals have large potential advantages in terms of erosion and lifetime by the continuous replacement of eroded material. Unlike tungsten or other solids they do not suffer from material degradations such as cracking [7], surface morphology changes [7] or blistering [8]. Furthermore, liquid metals are immune to neutron induced lattice damage [9,10] (though their substrates may be). Tin is considered to be a prospective candidate material due to its low melting point and high boiling point. It has a low evaporation rate and a high potential power exhaust capability, predicted to be up to 20–25 MW/m^2 [11,12]. Performance limits of tin in DEMO relevant conditions are primarily defined by the tin impurity level in the plasma core and thus by the sputtering/re-deposition rate. As tin is a high-Z material, contamination is a critical issue due to cooling by high radiation losses. Strong radiation losses with hollow or flat temperature profiles and impurity accumulation in the plasma core often lead to plasma disruptions [13,14]. For instance, tungsten (Z=74) concentration limit is $\sim 10^{-4}$, while for Sn (Z=50), its concentration limit should be closer to molybdenum (Z=42) which is $\sim 10^{-3}$ [15]. Therefore

without high re-deposition, strong core impurity flushing or low sputtering under reactor relevant conditions, any high-Z material is likely to lead to impurity levels incompatible with efficient fusion energy production.

In the present work we investigate sputtering and re-deposition of liquid tin under a ~50 eV high-flux plasma beam produced by the linear device Pilot-PSI [16] by the measurement of impurity concentrations by Cavity Ring-Down Spectroscopy (CRDS) for the first time. Typically impurity concentrations are determined from emission spectroscopy, but a limitation in such experiments is accurately determining the erosion and re-deposition rates. This requires detailed knowledge of the plasma species densities and energy distributions, along with rate coefficients for important processes such as ionization, recombination and charge exchange. As CRDS uses absorption of laser light the total line-integrated species number (in this case of ground-state Sn^0) can be unambiguously determined.

The experimental conditions and diagnostics are described in Section 2.1. A description of the CRDS system that was implemented is outlined in Section 2.2, while Section 2.3 describes the preparation of the Sn filled capillary porous system (CPS) targets [17-21]. Section 3 explains the experimental procedure and results, firstly in terms of characterization of the CRDS system (Section 3.1), and secondly an investigation of the erosion and re-deposition of the tin in argon (Ar) plasma (Section 3.2). Lastly the interpretation and implications of the obtained measurements are discussed in Section 4.

2. Setup and diagnostic description

2.1 Plasma exposure

Pilot-PSI (figure 1) is a linear plasma device capable of creating ITER relevant divertor conditions [22]. Experiments were conducted in Ar plasma. The total heat flux was evaluated by calorimetry, while the surface temperature was monitored with pyrometry (FAR Associates FMPI) and IR camera (FLIR SC7500MB, 4.5 kHz).
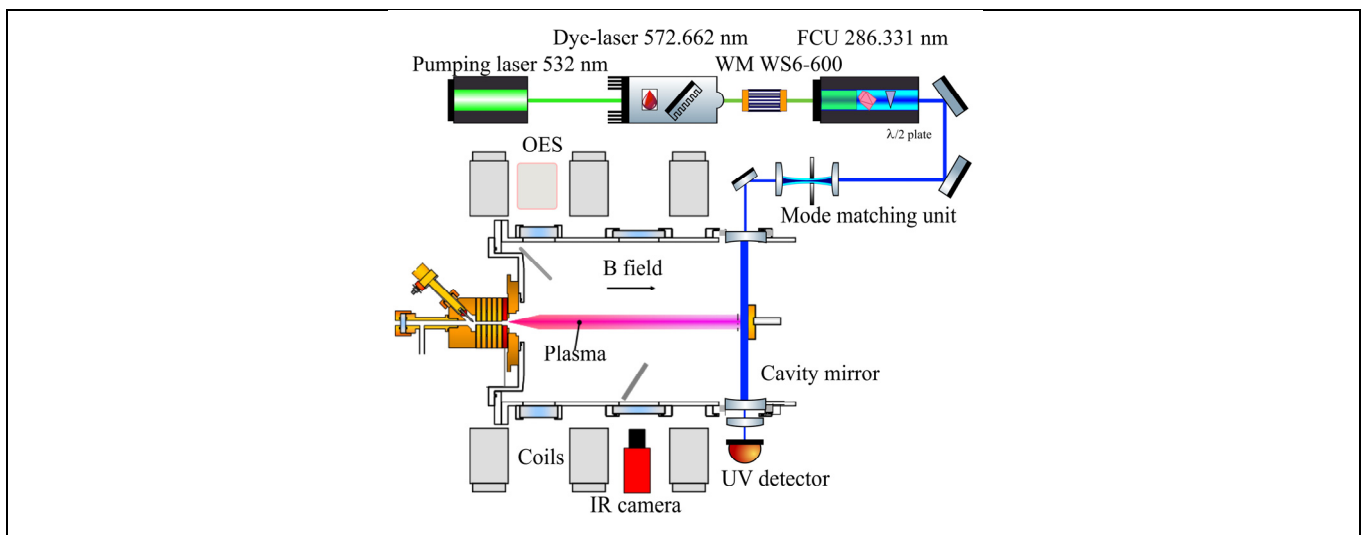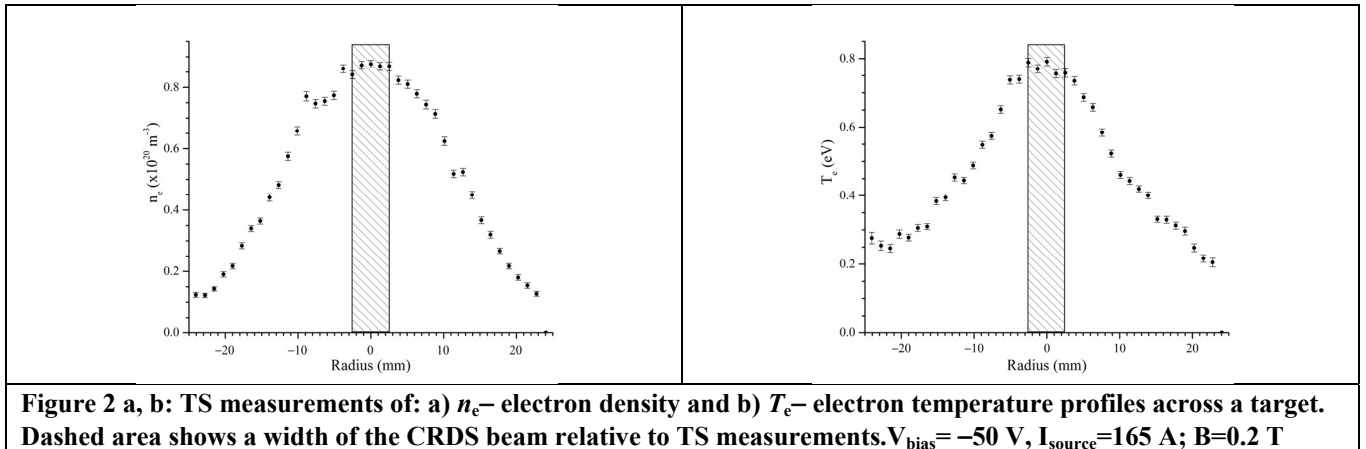

Figure 1: PILOT-PSI and Cavity-Ring-Down-Spectroscopy setup: a fundamental wavelength of Nd:YAG laser is converted by Sirah dye-laser and frequency coupler unit (FCU) into 286.331 nm laser beam. The wavelength is controled by a wavelength meter (WM) and polarisation is returned to s-pol by $\lambda/2$ plate. After multiple reflections from guiding mirrors the quality of the beam is restored by mode a matching unit before entering the cavity.

Electron temperature and density was estimated by Thomson scattering (TS) at the target [23]. As the CRDS system occupied the same ports as used for TS, these measurements had to be made separately from CRDS measurements during identical reference discharges. The TS laser beam was placed at the same distance from a sample surface, ~11 mm, as the CRDS beam. Typical electron density and temperature profiles are shown in figure 2 (a, b). Parameters of discharge shots in present experiments at the plasma centre were: T_e= 0.7–2.3 eV, n_e = 1.0–2.4x10^{20}m^{-3}; heat flux = 0.5–8 MWm^{-2}, particle flux = 1.6–2.7x10^{23}m^{-2} s^{-1}, magnetic field B = 0.2 T. Biasing was −50 V unless otherwise stated. Optical emission spectroscopy (OES) in the range of 294−580 nm was performed by two-channel spectrometer (Avantes ULS2048), focused at the target centre with a spot size of ~1 mm diameter and viewing at an angle of ~15° with respect to the target normal.

Figure 2 a, b: TS measurements of: a) n_e– electron density and b) T_e– electron temperature profiles across a target. Dashed area shows a width of the CRDS beam relative to TS measurements. $V_{bias}= -50$ V, $I_{source}=165$ A; B=0.2 T

2.2 Cavity-Ring-Down-Spectroscopy

The implementation of the Cavity-Ring-Down-Spectroscopy (CRDS) system was a distinguishing part of the work. CRDS is widely used for the detection of small amounts of impurities in a gas or plasma environment. One of the advantages of using such a technique in a plasma experiment is that it is independent of plasma parameters, clearly separating the signal from requiring knowledge of plasma species density and rate coefficients of the relevant plasma processes. This therefore avoids one of the main problems in optical emission methods to study plasmas by enabling the direct measurement of the absolute density of the chosen particle and particle state. It can also detect unexcited (and thus non-emitting) species outside of the plasma along the CRDS line-of-sight, unlike in emission spectroscopy. Furthermore, by using a tunable dye-laser a wide selection of species can in principle be detected depending on chosen wavelength. CRDS measures the rate of absorption of a light pulse confined in a high finesse optical cavity rather than the magnitude of its absorption. Therefore the diagnostic is also independent of pulse-to-pulse fluctuations of the laser, which can be an issue for other absorption techniques.

A detailed description of the CRDS technique can be found in [24], but a brief outline is given here for clarity. A sample is placed inside a high-finesse optical cavity. Then a laser pulse is coupled into the cavity at the wavelength of a chosen electronic transition of the species to be investigated. The light is reflected repeatedly between two highly reflective mirrors making up the cavity ends, and after each reflection a small portion of light is coupled out of the cavity to a detector. An exponential decay time (τ) for the light intensity is recorded such that the decay time will decrease relative to the decay time in vacuum (τ_0). This can be related to the average number density of the absorbing particles as:

$$\langle n \rangle = \frac{(\tau_0 - \tau)L}{c\,\tau_0 \tau \sigma d} \qquad (1)$$

where τ, τ_0 are ring-down times in the empty cavity and with the presence of the absorbing medium respectively, L is a total length of the cavity, c the speed of light, σ the absorption cross-section and d the length of the cavity occupied by the absorbent.

CRDS therefore effectively increases the path-length for absorption from a few cm or m for a single pass up to as much as several km. CRDS is thus a non-perturbing and extremely sensitive to even a small amount of impurity technique (absorption sensitivity up to 10^{-10}cm^{-1} [25] has been reported).

As Sn is predominantly sputtered or evaporated as a neutral a Sn^0 absorption line was selected. A wavelength of 286.331 nm Sn I (*5p^2* → *5p6s*) was chosen for the main absorption peak. This line is one of the persistent lines or raie ultime [26] of tin in ground state with high absorption rate [27-29]. Thus it is sensitive even to a small amount of tin in the discharge. Furthermore, in our experimental conditions there were no other species which absorb at this wavelength. Several persistent lines: 380.1 nm for Sn I observation and 533.23 nm, 556.19 nm and 558.88 nm for Sn II were chosen to monitor presence of those species in the discharge via spectrometer. These lines had a high intensity and therefore gave a clear qualitative indication of the amount of neutral tin and singly-ionized tin line-emission close to the target surface.

The implementation of the CRDS system had several stages which are shown in figure 1. A neodymium doped yttrium aluminum garnet laser (Nd:YAG, LAB-170, Spectra-Physics, 10 Hz, 10 ns, 0.5 mrad, 4.5 W) produced a

beam of 532 nm light, which was converted by a Sirah Cobra dye-laser (Rhadomine 6G) into 572.66 nm light (the pulse line width was 1.2 pm). Subsequently this was converted by a frequency coupler unit (FCU) with a SHG-260 KDP crystal into a 286.331 nm UV-beam of 50 mW power. The final wavelength was measured with a High finesse WS/6-UVU wavelength meter based on a Fizeau interferometer with absolute accuracy of 0.6 pm in the 192 – 370 nm wavelength range. The overall guiding distance between the Nd:YAG laser and the cavity was about 25 m.

Specially manufactured plano-concave mirrors were used to create a cavity of $L= 0.672$ m (Layertec R=0.997631 for s-polarized light at 286.5 nm). It was placed strictly tangential to the target surface at a distance of ~ 11 mm in front of the target position in Pilot-PSI. The tangential position was verified with additional laser beams relative positions simulating an incoming plasma beam and UV laser beam. Attention was devoted to the polarization of light after each conversion stage due to the relatively high drop in reflectivity of the mirrors depending on the polarization. The Nd:YAG laser and the dye-laser emitted s-polarized light but this was converted by the KDP crystal into p-polarization. This would lead to a strong drop of power after each reflection such that the cavity quality would strongly suffer as the reflectivity for p-polarization was R=0.940615. Therefore, after obtaining a UV beam we implemented a half-wavelength plate after the KDP crystal converting the light back to s-polarization. This enabled the maximum reflectivity of cavity mirrors to be utilized, minimizing power losses.

An additional complication was the necessity to choose the ultra-violet (UV) range for the measurements in order to use an absorption wavelength with a ground-state transition . The UV-multicoating of the mirror surface creates parasitic reflections and can decrease the beam quality. Another adverse effect is mode beating [30,31]. These issues were resolved with a mode matching unit. This consisted of an aperture and two UV fused silica plano-convex lenses (curvature radii of 27.6 mm and 9.2 mm). Using these a Gaussian-like beam of 5 mm diameter was obtained at the entrance to the cavity. The intensity of the laser light exiting the cavity was measured by a GaP detector (Thorlabs DET25K). This detector is insensitive to visible light which minimized to negligible levels the noise and the background signal from the plasma and surrounding environment. Tin coating of the cavity mirrors was excluded by an extra argon flushing flux on them during an experiment and tangential position of the cavity itself. In this way sputtered and evaporated particles are unlikely to reach the mirrors' surface. In addition we measured the ring down time in the empty cavity daily before an exposure and no degradation of reflectivity was observed.

Such a sensitive technique is commonly implemented in very steady and undisturbed environments, various examples are given in [24,30]. In this work CRDS was performed with sufficient decay time in the presence of many detrimental factors such as:

- a variable magnetic field
- pump vibrations
- mechanical shocks (evacuating and ventilation of the chamber)
- temperature variation (chamber temperature was changing from room temperature up to 120 °C during exposures)

This therefore gives a statistical noise such that signal was accumulated to give a normally distributed value whose variance was used to calculate the error bar of the signal.

2.3 Sample preparation

Samples with good wetting and a homogenous tin distribution over the sample volume were required for the Pilot-PSI experiments. Utilization of the capillary porous system (CPS) [32] in the target enabled exposures of a homogenous layer of liquid tin to the plasma beam. The CPS structure was produced by embedding a stack of tungsten and molybdenum meshes (with pores diameters 0.2 mm and 0.44 mm) in the melted tin (Goodfellow, purity 99.99%). Cups with outer diameter of 30 mm and inner diameter of 22 mm and depth 2 mm were filled with ~2.8 g of tin, which gave a good ratio of tin to CPS structure to avoid overfilling and splashing of liquid metal during exposures. Filling was made using a heater under vacuum conditions starting with a solid tin wire. At a temperature of about 800 °C tin demonstrated good wetting and homogeneous filling of a holder. To ensure uniform tin distribution throughout the sample volume tin was added stepwise between mesh layers and at the bottom of the holder. This ensured that after melting inter-layers of tin are created between meshes, avoiding voids such that capillary refilling of the surface can take place. Following the filling process samples were cooled to room temperature under vacuum to avoid contamination. Photographs of a typical sample surface are shown in

figure 3 (a, b) indicating that good wetting was achieved. Surface roughness was estimated from microscope pictures and weaving characteristics of the mesh to be <0.5 mm.

22 mm

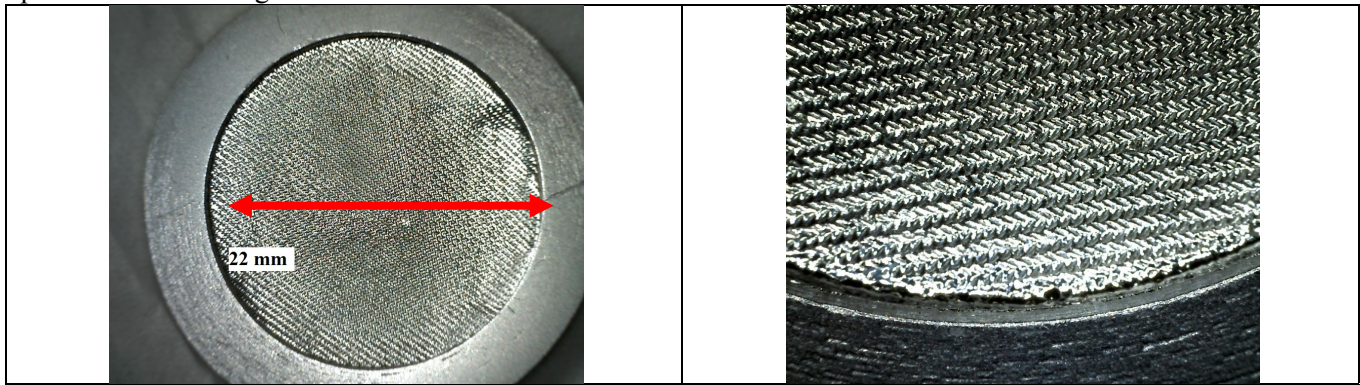**Figure 3: a – surface of a tin sample; b – wetting at the edge**

3. Measurements and experimental results

3.1 Characterization and verification experiments

We first made preliminary test shots in an argon discharge in the absence of a tin sample. The aim of these shots was to verify the decay time τ_0 of the laser signal and to ensure that the external negative factors listed in the Section 2.2 did not interfere with actual measurements. τ_0 was determined to be 159±2 ns. Following this a tin sample was exposed to an argon plasma flux of 2.3×10^{23} $m^{-2}s^{-1}$. Subsequent changes of signal both with biasing (significant tin sputtering) and without bias (absence of tin) were identified as shown in figure 4. Absence of sputtering and tin surface temperature below melting point ensured a negligible amount of tin during unbiased exposures. It was observed that there was a decrease of ring-down time measured at 286.331 nm from ~159 ns for unbiased samples to ~150 ns for biased samples. This decrease demonstrated the dependence of the signal on the presence of tin atoms due to sputtering (surface temperature was below the melting point here also). Following this a wavelength scan with resolution of 20 pm was carried out with fixed bias of −50 V. The result of this scan (figure 5) demonstrated that there is an maximum absorption at the chosen peak 286.331 nm. Calculation of a ring-down time was made by averaging over 400 direct measurements. The standard deviation of the normal distribution in τ due to random jitter, vibrations in the system etc. was used to define the error bar.
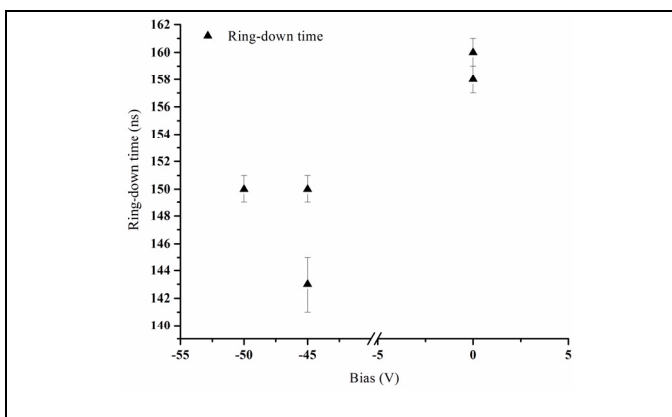

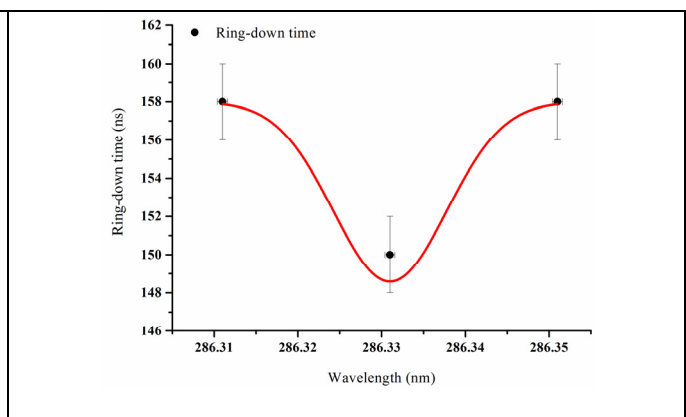| **Figure 4: Ring-down time with and without bias for two different biases and two different plasma fluxes.**	**Figure 5: Ring-down time at the resonant (286.331 nm) and off-resosnant (step of 20 pm) wavelengths. Red curve shows a simulated line profile and is for guiding purpose only.**

3.2 Results of the measurements

A continuous exposure of the tin sample with a gradual increase of source power at a fixed bias of −50 V was carried out. The difference between CRDS signal in the presence of tin and without it was again clearly distinguishable when the bias was switched on. This moment and a subsequent decrease in τ is shown by a dashed arrow in figure 6. This figure represents simultaneous evolution of the ring-down time, sample temperature and Sn I and II lines emission during the discharge. At a given bias an increase in source power leads to a stronger

sputtering of the target (seen in the increment of the Sn I line at 380.1 nm), an increase of tin in the cavity and the subsequent decrease of the ring-down time. The gradual steps in the source power are well correlated to the temperature increase and Sn I, II line intensity changes at temperatures below 950 °C (figure 6, 7). However above 950°C rapid increases in the Sn I emission line match a strong increase in the temperature curve while the source power, the Sn II (533.26 nm) emission and the target current do not demonstrate such a fast variation.
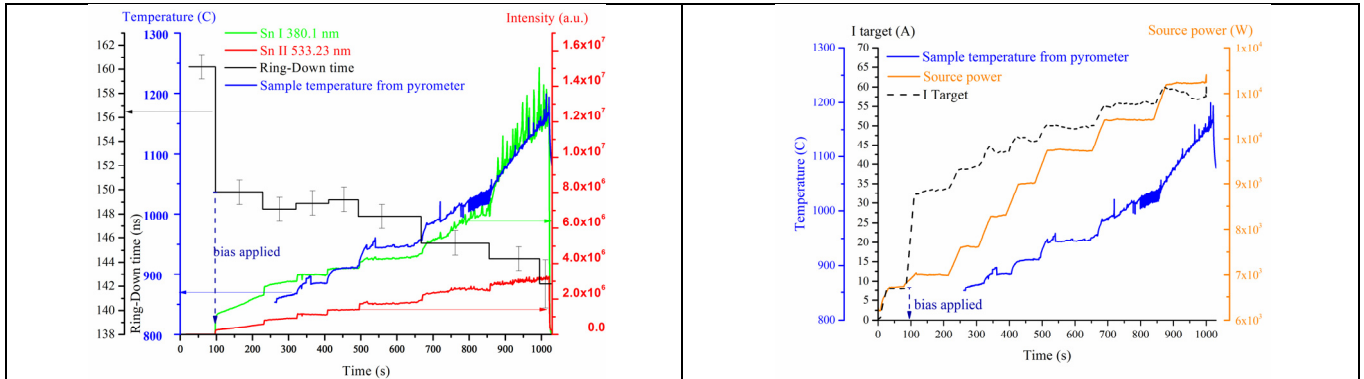

Figure 6: Evolution of ring-down time, sample temperature and Sn I line intensity during plasma exposure. Solid arrows show correspondence between graph and its axis.	Figure 7: Target current, source power and sample temperature during plasma exposure

Estimations from Langmuir's law of evaporation [33] predict that only at around 1200 °C should the evaporation rate start to be dominant over sputtering but temperature enhanced erosion (TEE) below that temperature beginning at around 900 °C was previously reported under similar conditions [34], consistent with our observations here. The increasing intensity line contribution above 900 °C therefore should be interpreted as TEE as reported in many other works [35-38]. Figure 8 represents a ratio between line intensities as a function of the sample temperature. Magnitudes of three persistent lines of Sn II (553.23 nm, 556.19 nm and 558.88 nm) are shown with respect to neutral Sn I line (380.1 nm). It is worth to mention main features in this figure:

1. There are two clearly distinguishable regions. Below 1000 °C ratios steadily increase, but above this temperature all three ratios decline. This implies that a temperature dependent phenomena e.g. TEE [35-38], becomes more prominent near 1000 °C.
2. In our electron temperature range of interest (0-10 eV) the ionization rate-coefficient is a strong function of temperature and only weakly independent on density, while the ratio of emission is proportional to n_e and the rate coefficient. As source power is increased during the experiment the main effect is to increase the plasma density while not strongly changing the electron temperature. Therefore, in sputtering-dominated plasmas (<1000 °C) we can interpret the increasing ratio as due to the increase in density leading to higher rates of ionization.
3. Above 1000 °C TEE becomes significant, leading to significantly more Sn in the plasma. This can lead to a moderate cooling effect and thus a decrease in the ionization rate which more than compensates for the increased n_e as the source power is further raised, leading to a drop in the line-intensity ratio.
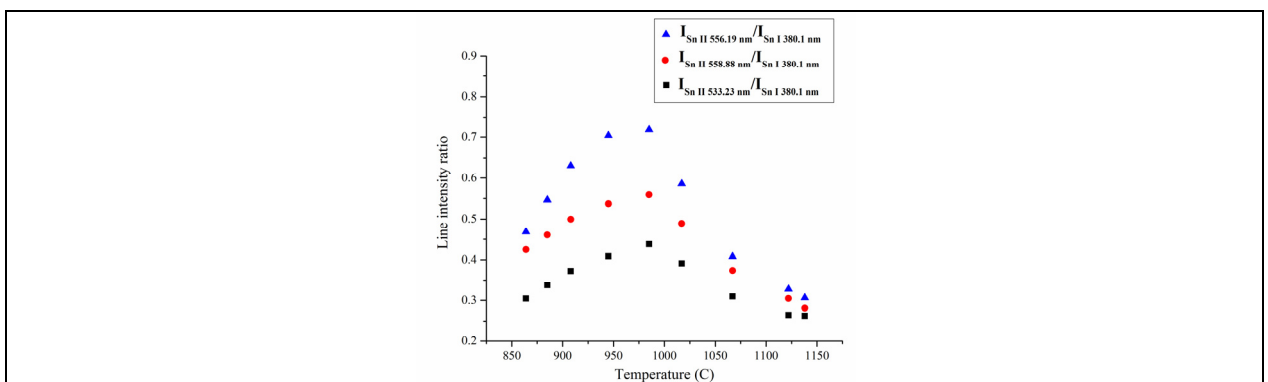

Figure 8: Line intensities ratio: intensities of three persistent lines of Sn II (533.23 nm, 556.19 nm and 558.88 nm) with respect to Sn I line 380.1 nm

4. Discussion

To determine the re-deposition rate we calculate how much tin would be expected to be sputtered from the sample and compare our measurements with theoretical values. It is essential to consider the geometry of the beam and the subsequent dimensions of the CRDS scanned volume; i.e. to calculate not only the number of particles that leave the surface but the number of particles in the probed volume 11 mm from the sample at a given moment. The second step is converting it to the absolute number of particles in the probed volume that should be detected by CRDS.

The eroded flux is composed of sputtered and evaporated particles, neglecting for now the contribution of anomalous temperature-enhanced sputtering (thus giving a lower estimate). Sputtered flux depends on incoming ion flux and sputtering yield, while evaporation depends only on the surface temperature. From TS measurements we can obtain rather accurately the incoming flux of argon ions along the target surface assuming $T_e \approx T_i$. But there is an uncertainty in the sputtering yield magnitude. At low energies (below 100 eV) there are mainly sputtering yield calculations based on codes such as TRIM or SRIM. SRIM-2000/03 gives high value artifacts as shown by Wittmaack in [39]. The liquid state of the sputtered surface should also be taken into account. General corrections for TRIM are given in [40] and specifically for liquid tin in [41]. Furthermore, at low-energies the distribution of sputtered particles significantly deviates from a cosine-law under perpendicular incoming flux [42,43]. We estimated the maximal amount of tin atoms in the CRDS observation volume assuming that sputtered particles can arrive to the scanned volume without collisions, re-deposition or changing ionization state. The next assumption is that the flux of sputtered tin is homogeneously distributed in a solid angle of 2π. Then the flux through a rectangle with sides equal to CRDS beam diameter of 5 mm and to the width of the chamber (486 mm) is given by:

$$F_{out}^{sput} = \iint \int_{\theta_1(y)}^{\theta_2(y)} \frac{Y F_{in}(x,y)}{A} \sin(\theta)\mathrm{d}\theta\mathrm{d}x\mathrm{d}y \ (2a)$$

$$F_{out}^{evap} = \iint \int_{\theta_1(y)}^{\theta_2(y)} \frac{F_{evap}(x,y)}{A} \sin(\theta)\mathrm{d}\theta\mathrm{d}x\mathrm{d}y \ (2b)$$

$$F_{in}(x,y) = F_{in}(x=0, y=0)\exp(-0.5(x^2+y^2)/\sigma_{beam}^2)(3a)$$

$$F_{evap}(T,x,y) = F_{evap}(T(x=0,y=0))\exp(-0.5(x^2+y^2)/\sigma_{beam}^2) \ (3b)$$

where F_{out}^{sput} and F_{out}^{evap} are the total outcoming fluxes through the rectangle due to sputtering and evaporation respectively, A the rectangle area, θ the azimuthal angle, Y the sputtering yield for tin at E_{ion}=50 eV taken from [42] to be equal to 0.1. This value is the highest that can be extracted from [41,42]. $F_{in}(x,y)$ is the Gaussian distribution function of the incoming plasma flux, $F_{evap}(x,y,T)$ the Gaussian distribution function of the evaporated flux of tin atoms along the sample surface, $F_{evap}(T(x=0, y=0))$ was obtained from two simple formulas: $F=nv$ and ideal gas law $p=nkT$, where v is thermal velocity of tin atoms and p was calculated as vapor pressure from [44], and σ_{beam} is the standard deviation of the plasma beam profile. The integration was made numerically in MATLAB, calculating outgoing flux from each elemental square $a=\Delta x \Delta y$ and its contribution in the solid angle defined by probed volume geometry (figure 9).
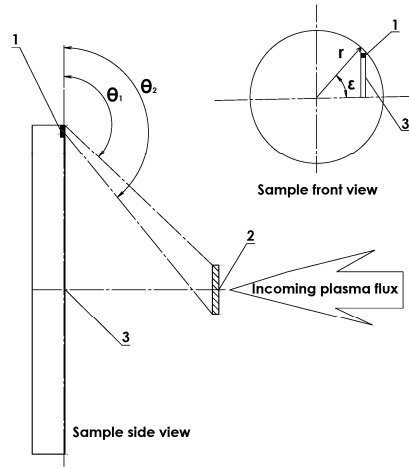
Figure 9: Schematic view of the geometry for numerical integration: 1 – elementary square, 2 – cross section of scanned area, 3 – sample elementary layer

Obtained fluxes should be divided by v which is a velocity of tin atoms. Sputtered tin atoms leave the surface typically with maximum half of the surface-binding energy [42], which means that they have energy of $\langle E \rangle =$ 1.56 eV [45] and subsequent velocity v_0, while evaporated particles have thermal velocity (v_{th}). Thus substituting all values above into simple equation $N_{calc} = \left(F_{out}^{sput} / v_0 + F_{out}^{evap} / v_{th} \right) \times V$, where V is the volume of the cavity we can expect the number of neutral tin atoms to be detected by CRDS equals to N_{calc}=5.5x10^{11}–1.2x10^{12} for the range of the fluxes applied here as the source power was varied (red circles in figure 10). The contribution of evaporated particles to the total number of eroded particles varies from 0.2%–13%. This suggest that already ~10% of evaporated particles in the total flux may play a significant role in the emission line ratio observed in figure 8 (see end of the section 3.1). This value is the upper limit because we assume no re-deposition, ionization and the maximum possible Y.

The next step is to determine the number of particles via the CRDS method. A general overview and the relevant equations can be found in literature such as [24,30,31]. We note here corrections made to the basic equations to obtain the average tin density and the subsequent number of measured particles $N_{meas} = \langle n \rangle V$. We consider a narrow frequency interval, thus the frequency dependence of the cross-section and the mirror reflectivity can be neglected. Moreover, if we create such conditions (a specifically chosen wavelength and presence of only one absorptive species in the cavity), then the absolute density value $\langle n \rangle$ can be calculated with equation (1).

The tin absorption cross-section for UV radiation at 286.331 nm has not been precisely measured. However Hilborn [46] showed that a cross-section can be calculated as:

$$\sigma(286.331) = \frac{g_2}{4g_1} \lambda_{21}^2 g(\omega) A_{21} \qquad (4)$$

where $g_{1,2}$ are statistical weights of the first excited and ground state of tin respectively, λ_{12} the wavelength of absorbed light, $g(\omega)$ the line profile, A_{21} the Einstein coefficient of spontaneous emission (reference values are taken from [26]). Fast neutrals imply that Gaussian broadening is dominant (at least 5 times bigger) over natural and Stark broadening. Thus assuming a Gaussian line profile with a width determined by the particle velocity v_0 as above we obtain σ =3.5x10^{-17} m^2. Using equation (1) we therefore find average densities in the range $\langle n \rangle =$ 5–10x10^{13} m^{-3} and N_{meas}=5.7–9.9x10^8.

As one can see the number of neutral tin atoms measured by CRDS represented in figure10 even with error bars are significantly lower (three orders of magnitude) than from calculations above. This therefore suggests that at least one of the above assumptions are not valid. Tin atom velocity and subsequent absorption cross-section should have the largest influence on the measured values along with ionization rate of tin and the magnitude of sputtering yield at low energies (near threshold). Below we consider each of those parameters separately and give an evaluation of their importance to the measurements and estimations.
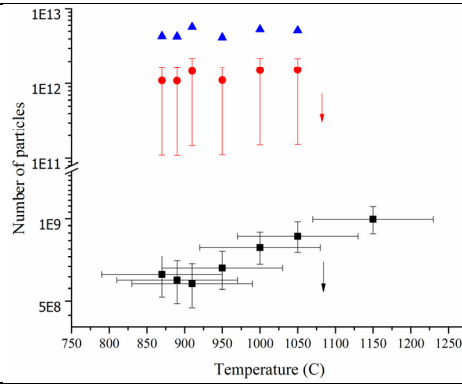
Figure 10: Dependence of the number of tin atoms calculated based on measured ring-down time on sample temperature: black squares –number of Sn atoms measured by CRDS, red circles–number of Sn atoms calculated using equation (2 a, b) with particle velocity defined by surface binding energy, blue triangles –number of Sn atoms calculated using equation (2 a,b), but with smaller particle velocity defined by evaporation. Red arrow shows effect of decreasing Y and uncertainty in the ion energy on estimated values. Black arrow shows an effect of temperature reduction in Gaussian line profile calculation on measured values.

A vast database of experimental sputtering yields for energy ranges down to 100 eV is given in [42]. At low energies <100 eV there are mostly calculations [42] and theoretical predications [47, 48]. Some works have attempted to increase the accuracy of calculated yields by SRIM and TRIM [39] at these energies, but still below 100 eV rather big error bars for tin sputtering remain. Sigmund suggested at least 50% error in the Y magnitude due to certain effects in the low projectiles energy range [47] and despite more recent advances in sputtering calculations we take this as a conservative estimate. This error was therefore used in the figure 10 to calculate error bars. In [39] Wittmaack showed that SRIM simulations at low (~1 keV) projectile energies give overestimated results for sputtering yield. These overestimated yield calculations appear irrespective of code input parameters such as the surface binding, the bulk binding, and the displacement energy. In particular he observed that calculated and experimental yields can be $Y_{\mathrm{SRIM}}/Y_{\mathrm{expt}} > 3.4$ at 1 keV impact energy for $Z_1/Z_2 < 0.5$ where Z_1, Z_2– atomic numbers of the projectile and the target respectively. Thus this effect may be even more prominent at lower energies. Biasing in our experiments was −50 V and $Z_{\mathrm{Ar}}/Z_{\mathrm{Sn}} = 0.36$ indicating an overestimate of the sputtering yield is likely. In addition Grossman et al. [40] described a weak dependence of the yield calculated by TRIM and SRIM codes on surface tension at elevated temperatures in the liquid phase of a metal. Lastly there is an uncertainty in the ion energy due to the error in determining T_e and in estimating the floating potential. As the yield curve is very steep [42] in this region any uncertainties result in a very high variation of the sputtering yield in the low energy range. A decreased sputtering yield will result in lower expected N_{calc} values of sputtered tin, but cannot likely be more than maximally one order of magnitude. This effect is shown by a red arrow in figure 10 and included in a lower error bar.

Secondly, the temperature of tin atoms can also have a significant impact on expected and measured N_{calc} and N_{meas}. The velocities that we have used after calculating outgoing flux (equation 2a and 2b) were defined by the surface binding energy and thermal velocity for evaporated particles. If evaporation dominates then the velocity would be thermal for all outgoing particles and thus much lower, but in this case N_{calc} would be higher as it is proportional to v^{-1}. The effect of decreasing Sn atoms velocity such that all particles would be thermal on expected number of neutral tin atoms is represented by blue triangles (figure 10). The temperature of tin atoms is also implicitly included in the cross-section calculation via line profile function $g(\omega)$ (see equation 4). A Gaussian line profile (GLP) was used in above calculations. As this line profile was estimated using the temperature of tin atoms defined by a half of the surface binding energy [42] it should be the upper estimate when expressing N_{meas}. A temperature reduction in GLP calculation would increase the magnitude of absorption cross section at λ_{21} and subsequently decrease the N_{meas}. This influence is shown by a black arrow in figure 10. Summarizing different factors discussed above we can conclude that a decrease in tin atom temperature will have following effects:

- N_{meas} will decrease as it is $\propto \sqrt{T_{Sn^0}}$ (black arrow in figure 10).

- N_{calc} will increase as it is $\propto 1/\sqrt{T_{Sn^0}}$ (blue triangles in figure 10)

Therefore this would act overall to increase the expected discrepancy between theory and observation.

Thirdly, we discuss plasma entrainment which can also play significant part in the reducing the detected neutral tin amount. Mott and Massey [49] developed a theory of interaction between ions and atoms at low energies. They give an expression (in CGS) for a momentum transfer cross section in such interactions:

$$\sigma_{mt} = 2.210\pi\sqrt{\alpha Z^2 e^2 / 2E} \qquad (5)$$

where α is the atom polarizability, Ze the ion charge and E the relative kinetic energy of the interacting atom and ion. Substituting tin polarizability of 6×10^{-30} m^3 [50] we obtain $\sigma_{mt}^{evap} = 4.4\times10^{-19}$ m^2 and $\sigma_{mt}^{sput} = 3.1\times10^{-19}$ m^2. These values correspond to tin atom energies determined by the surface temperature (evaporation) or the sample surface binding energy (sputtering). A characteristic path of this momentum transfer from argon ions of density n_i can be estimated by a simple equation $\lambda = 1/\sigma_{mt}n_i$ which gives $\lambda_{mt}^{evap} = 8$ mm and $\lambda_{mt}^{sput} = 12$ mm. Calculated paths are comparable to the position of the CRDS beam which was placed at ~11 mm from the target surface. This implies that argon ions will efficiently push back neutral tin atoms towards the sample. Thus they can get re-deposited before reaching the scanned volume. This effect can lead to 3-5 times less detected particles than estimated from evaporation and sputtering.

Lastly, we discuss the ionization of tin. As only neutral Sn can be detected by the CRDS a high level of ionization would lead to a lower value than expected of N_{meas} relative to N_{calc}. The detection of ionized tin was performed by spectrometer observing several persistent lines [26] of Sn II. Figure 6 shows the intensities of the lines of ground state Sn I 380.09 nm, ionized Sn II 533.23 nm and ring-down time during the discharge, while figure 8 clearly indicates a significant population of Sn II leading to line emission ratios relative to Sn I of order 1. We wanted to estimate relative populations of ionization states n_{i+1}/n_i. We first make estimates from equilibrium calculations.

As a first assumption we considered Pilot-PSI's high density plasma beam in local thermal equilibrium (LTE) and used the Saha equation:

$$\frac{n_{i+1}}{n_i} = \frac{2g_{i+1}}{g_i n_e}\left(\frac{2\pi m_e kT_e}{h^2}\right)^{3/2}\exp\left(-\frac{\chi}{kT_e}\right) \qquad (6)$$

where g_{i+1}, g_i are statistical weights of levels $i+1$ and i respectively, m_e, n_e, T_e the electron mass, density and electron temperature respectively, k, h Boltzman and Plank constants respectively, χ energy difference between levels i and $i+1$. Substituting parameters of the plasma beam and calculating this ratio for the first tin ionization potential 7.34 eV [26] i.e. for a relative population between ground state Sn I ($5s^2 5p^2\,^3P_0$) denoted as n_0 and the first ionized state Sn II ($5s^2 5p\,^2P_{1/2}$) denoted as n_1 we obtain ratio $n_1/n_0 \approx 4\times10^4$ meaning that tin should be fully ionized in LTE. However, according to the McWhirter criterion [51] the density of the plasma is not sufficient for LTE to be a strict description ($n_e > 7.7\times10^{22}$ m^{-3}). It should be noted that such strong ionization would lead to an even smaller number of particles than we measured (i.e. a larger discrepancy) and so this is likely an overestimate. We can also calculate populations from semi-empirical rate coefficients [52]. In this case LTE is no longer assumed, but that the density and opacity is low enough that only electron mediated ionization and recombination from and to ground states are the dominant processes. This is essentially equivalent to local coronal equilibrium (LCE) between ionization stages. In this case:

$$\frac{n_{k+1}}{n_k} = \frac{\langle\sigma_{k,k+1}v\rangle}{\sum_l\langle\sigma_{k+1,ki}v\rangle} \qquad (7)$$

Where n_{k+1}, n_k are the ground state populations of ionization stages $k+1$, k; $\langle\sigma_{k,k+1}v\rangle$ the ionization rate coefficient from the ground state, and $\langle\sigma_{k+1,ki}v\rangle$ is the total recombination rate coefficient to neutral atom level i (for detailed expressions see [52]). Calculation of rate coefficients in this approximation using equation 7 gives a value of $n_1/n_0 \approx 500$, i.e that the ionized population is again very large. Such large ionization fractions also seem compatible with other experiments. For example Hajjar et al. [53] observed high ionization of neutral

aluminum atoms to the Al^{2+} state by helium plasma in similar experimental conditions to ours.

In both of the above cases equilibrium conditions are assumed, which may not be true close to the plasma surface as the eroded particles require a finite time to equilibrate in the system. Furthermore, both are purely theoretical calculations. Therefore we use the measured line intensity ratios of figure 8 to attempt a more accurate evaluation. We take two cases corresponding to two density conditions LTE where Boltzmann relationships between all levels should hold and secondly LCE between levels where excitation is electron mediated and de-excitation is through spontaneous emission. These correspond to high density and low density conditions respectively, while our experiment should lie somewhere between these two extremes.

In both cases we can define relationships between the excited and ground state populations of neutrals (i=0) and ions (i=1) as

$$\frac{n_{i*}}{n_i} = \frac{g_{i*}}{g_i} \exp\left(-\frac{\Delta E_{ii*}}{kT_e}\right) \qquad (8a)$$

for the Boltzmann case, where n_{i*} and n_i are populations of the excited and the ground state i respectively, g_i, g_{i*} are the statistical weights of the ground and excited levels and ΔE_{ii*} the energy difference between them. For LCE the relationship is given as [52]:

$$\frac{n_{i*}}{n_i} = \frac{n_e \langle \sigma_{ii*} v \rangle}{\sum_j A_{i*j}} \qquad (8b)$$

where $\langle \sigma_{ii*} v \rangle$ is the excitation rate coefficient, and A_{i*j} the Einstein coefficient from the excited state to decay to level j. Now we calculate the same relative population between ground state Sn I ($5s^2 5p^2$ $^3P_0$) and the first ionized state Sn II ($5s^2 5p$ $^2P_{1/2}$) but with an intermediate evaluation of relative population between excited and ground states of Sn II and Sn I. n_{i*} value for respective species is obtained from measured intensities (see figure 8) and applying equation:

$$\frac{n_{1*}}{n_{0*}} = \frac{A_{0k}^0 I_{1*}}{A_{1p}^1 I_{0*}} \qquad (9)$$

where n_{1*} and n_{0*} are the populations of excited levels of Sn II and Sn I respectively, A_{0k}^0, A_{1p}^1 the Einstein coefficients for transitions from the observed excited to de-excited states, I_{1*} and I_{0*} intensities of observed lines of Sn II and Sn I. The equation for $\langle \sigma_{ii*} v \rangle$ is given in [52] substituting equation (8a) or (8b) into equation (9) and rearranging the ratio n_1/n_0 gives values from 0.08 to 0.13 for Boltzman case and values from 0.05 to 0.12 for the LCE case, depending on the Sn II line under consideration (see figure 8) and magnitude of electron density during the exposure. As these numbers are relatively consistent we can assume values are close to these numbers at the observation position of the OES. This again indicates ionization is important, but not sufficient to entirely comply with the measurements. However, as the observation position of the CRDS is 11 mm further from the surface compared to OES we may expect higher ionization ratios at this point. An intermediate ratio between the calculated and estimated values here of a factor ~10-20 thus seems plausible. Figure 11 demonstrates a strong dependence of the ionization rate, rate coefficients used in equations 7 and 8b on the electron temperature. This indicates the importance of an equilibrium electron temperature in scanned volume and near sample surface as mentioned above.
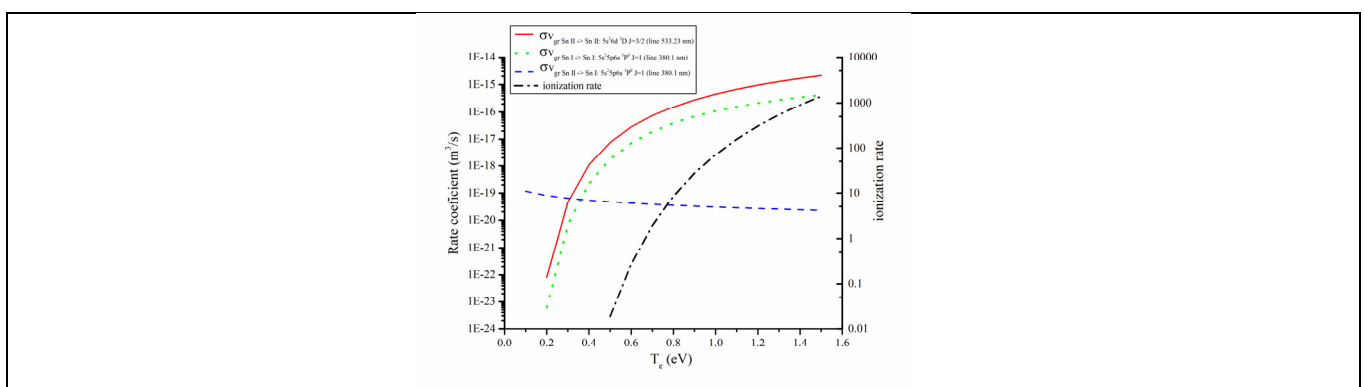

Figure 11: Calculated rate coefficients for excitation, 3-body recombination and ionization rate using expressions

Overall we may consider the contribution of sputtering yield error, entrainment effect and ionization most critical. While a lower sputtering yield could lead to a reduction by up to a factor 10 in N_{calc}, entrainment and ionization can be used to mostly explain the low N_{meas}. Therefore combined effect of sputtering yield overestimation, plasma entrainment and high ionization will explain discrepancy between measured and predicted number of particles. Entrained neutrals will be expected to mostly return to the target. As ionized particles are trapped in the magnetic field most ionized tin species should also be drawn-back to the negatively biased target by the sheath field in the case of prompt ionization or entrained in the plasma flow due to the large flow velocity towards the target [54, 55] and re-deposited. It should be noted that this depends mostly on electron temperature and density rather than ion species, and thus would also be applicable to dominantly light-ion plasmas, such as in fusion reactors, rather than pure argon plasmas as here.

A ratio between CRDS Sn I measured number of neutral tin atoms (figure 10) and calculated above sputtered tin atoms is given by $N_{meas}^{SnI} / N_{calc}^{SnI} \sim 0.2 - 2\%$. Given that geometric losses are accounted for as well as uncertainties in both the measured and predicted neutral densities this implies that physical processes must be important. Our calculations show that both ion-neutral friction leading to entrainment and ionization can play a role and we attribute the observed discrepancies to these processes. This implies that ~98-99.8% of sputtered tin is either ionized or entrained and thus would be predominantly re-deposited. The implication of this is that under high-flux plasma conditions a high re-deposition rate can be expected, so that in a future fusion reactor such as DEMO this would effectively increase the tolerable gross erosion and thus in evaporation-dominated regimes the operational temperature window. This would also reduce the requirements for the tin resupply rate to the surface and thus the required flow rate, which reduces engineering considerations.

V. Conclusion

CRDS was successfully implemented to measure neutral tin density sputtered from samples exposed to high flux beam of $1.6–2.7 \times 10^{23}$ m^{-2} s^{-1} argon ions. Samples were made of molybdenum substrate with CPS structure produced as a stack of tungsten and molybdenum meshes embedded in the melted tin. The number of detected of sputtered tin atoms varied from 5.7 to 9.9×10^8 compared to theoretical expectations of $5.5 \times 10^{11}–1.2 \times 10^{12}$ assuming no re-deposition or ionization, indicating these processes are important. Calculations and optical emission observations show that both entrainment and ionization can play a role in the reduction and this high ratio implies that ~98-99.8% of the eroded Sn atoms can be ionized and re-deposited. This indicates that core impurity contamination from tin surfaces exposed to high density plasmas such as would be expected in the DEMO divertor may be more tolerable due to the high re-deposition rate. Large re-deposition fractions may also increase the effective temperature range for a tin PFM (and thus power handling capability) compared to assumptions of negligible re-deposition.

Bibliography:

[1] Romanelli F, Barabaschi P, Borba D, Federici G, Neu R, Stork D, Horton L and Zohm H 2012 Fusion Electricity *A roadmap to the realisation of fusion energy*

[2] Fetzer R, Igitkhanov Y and Bazylev B 2015 Efficiency of water coolant for DEMO divertor *Fusion Eng and Design* **98–99** 1290–93

[3] You J H et al. 2015 Conceptual design studies for the European DEMO divertor: Rationale and first results *Fusion Eng. Des.* http://dx.doi.org/10.1016/j.fusengdes.2015.11.012

[4] Maisonnier D et al. 2007 Power plant conceptual studies in Europe *Nucl. Fusion* **47** 1524–1532

[5] You J H et al. 2016 European DEMO divertor target: Operational requirements and material-design interface, *Nuc. Mat. En.* http://dx.doi.org/10.1016/j.nme.2016.02.005

[6] Kallenbach A et al. 2013 Impurity seeding for tokamak power exhaust: from present devices via ITER to DEMO *Plasma Phys. Control. Fusion* **55** 124041

[7] Budaev V P et al. 2015 Tungsten recrystallization and cracking under ITER-relevant heat loads *Jour. Nucl. M.* **463** 237–40

[8] Ueda Y, Coenen J W, De Temmerman G, Doerner R P, Linke J,Philipps V and Tsitrone E 2014 Research status and issues of tungsten plasma facing materials for ITER and beyond *Fus. Engin.&Des.* **89** 901–6

[9] Van Renterghem W and Uytdenhouwen I 2016 Investigation of the combined effect of neutron irradiation and electron beam exposure on pure tungsten *Jour. Nucl. M.* **477** 77-84

[10] Fukuda M, Kumar N A P K, Koyanagi T,Garrison L M , Snead L L, Katoh Y and Hasegawa A 2016 Neutron energy spectrum influence on irradiation hardening and microstructural development of tungsten *JNM* **479** 249-54

[11] Coenen J W, De Temmerman G, Federici G, Philipps V, Sergienko G, Strohmayer G, Terra A, Unterberg B, Wegener T and Van den Bekerom D C M 2014 Liquid metals as alternative solution for the power exhaust of future fusion devices: status and perspective *Phys. Scr.***T159** 014037

[12] Morgan T W, Vertkov A, Bystrov K, Lyublinski I, Genuit J W and Mazzitelli G 2016 Power handling of a liquid-metal based CPS structure under high steady-state heat and particle fluxes submitted to Nuclear Materials and Energy *Preprint of Paper to be submitted for publication in 22nd International Conference on Plasma Surface Interactions in Controlled Fusion Devices (22nd PSI)*

[13] Hawryluk R J et al. 1979 The effect of current profile evolution on plasma-limiter interaction and the energy confinement time *Nucl. Fusion***19** 1307-17

[14] Nakamura H, Ando T, Yoshida H, Niikura S, Nishitani T,and Nagashima K 1988 Divertor experiment on particle and energy control in neutral beam heated JT-60 discharges *Nucl. Fusion* **28** 43-52

[15] Loarte A et al. 2007 Power and particle control *Nucl. Fusion* **47** S203–63

[16] van Rooij G J et al 2007 Extreme hydrogen plasma densities achieved in a linear plasma generator *App. Phys. Let.***90** 121501-3

[17] Lyublinski I, Vertkov A, Mirnov S and Lazarev V 2015 Protection of tokamak plasma facing components by a capillary poroussystem with lithium *J. of Nucl. Materials* **463** 1156–59

[18] Apicella M L, Lazarev V, Lyublinski I, Mazzitelli G, Mirnov S and Vertkov A 2009 Lithium capillary porous system behavior as PFM in FTU tokamak experiments *J. of Nucl.Mat.* **386–388** 821–3

[19] Mirnov S 2010 Experiments at the T-11M device in support of the tokamak concept with closed Li cycle *Fusion Eng. and Design* **85** 919–23

[20] Khripunov B I, Petrov V B, Shapkin V V, Antonov N V, Pleshakov A S, Rupyshev A S, Prokhorov D Yu, Evtikhin V A, Lyublinsky I E, Vertkov V V 2003 Lithium surface operating under steady-state power load *Fusion Eng. and Design* **65** 449-54

[21] Lyublinski I E and Vertkov A V 2010 Experience and technical issues of liquid lithium application as plasma facing material in tokamaks *Fusion Eng. and Design* **85** 924–29

[22] De Temmerman G, Zielinski J J, van Diepen S, Marot L and Price M 2011 ELM simulation experiments on Pilot-PSI using simultaneous high flux plasma and transient heat/particle source *Nucl. Fusion* **51** 073008

[23] van der Meiden H J et al. 2008 High sensitivity imaging Thomson scattering for low temperature plasma *Rev. Sci. Instrum.***79**, 013505

[24] Scherer J J, Paul J B, O'Keefe A, and Saykally R J 1997 Cavity Ring down Laser Absorption Spectroscopy: History, Development and Application to Pulsed Molecular Beams *Chem. Rev.* **97** 25-51

[25] Romanini D and Lehman KK 1993 Ring-down cavity absorption spectroscopy of the very weak HCN overtone bands with six, seven, and eight stretching quanta *J. Chem. Phys.***99** 6287 http://dx.doi.org/10.1063/1.465866

[26] Sansonetti J E and Martin W C 2005 *NIST: Handbook of Basic Atomic Spectroscopic Data American Institute of Physics* (*J. Phys. Chem. Ref. Data*) Vol. 34 No. 4 DOI: 10.1063/1.1800011

[27] Agazzi E J 1965 Determination of Tin in Hydrogen Peroxide Solutions by Atomic Absorption Spectrometry *Analyt. Chem.* **37 Nr. 3** 364-6

[28] Muradov V G 1979 Measurement of the saturated vapor pressure of *tin J. of Applied Spectroscopy***30 Nr. 2** 154-8

[29] Zumstein R V 1926 The absorption spectrum of tin vapor in the ultraviolet *Phys. Rev.***27** 150-6

[30] G Berden and R Engeln *Cavity Ring-Down Spectroscopy: Techniques and Applications* 2009 ed (ISBN: 978-1-4051-7688-0, Wiltshire, UK, Wiley-Blackwell) p 8

[31] Paldus B A, Harb C C, Spence T G, Wilke B, Xie J, Harris J S and Zare R N 1998 Cavity-locked ring-down spectroscopy *J. Appl. Phys.***83 Nr. 8** 15 3991-7

[32] Evtikhin V A, Vertkov A V, Lyublinski I E, Khripunov B I , Petrov V B and Mirnov S V 2002 Research of lithium capillary-pore systems for fusion reactor plasma facing components *JNM* **307–311** 1664–69

[33] Langmuir I 1932Vapor pressures, evaporation, condensation and adsorption *J. Am. Chem. Soc.***54**

(7) 2798–832

[34]   Morgan T W, van den Bekerom D C M and De Temmerman G 2015 Interaction of a tin-based capillary porous structure with ITER/DEMO relevant plasma conditions *J. of Nucl. Materials* **463** 1256–59

[35]   Doerner R P, Baldwin M J, Krasheninnikov S I and Whyte D G 2003 Behavior of high temperature liquid surfaces in contact with plasma *JNM* **313–316** 383–387

[36]   Roth J and Moller W 1985 Mechanism of enhanced sputtering of carbon at temperatures above 1200 C *Nucl. Instr. and Meth. in Phys. Res.* **B 7/8** 788-92

[37]   Conn R W, Doerner R P, Sze F C, Luckhardt S , Liebscher A, Seraydarian R and Whyte D G 2002 *Nucl. Fusion* **42** 1060–66

[38]   Allain J P, Coventry M D and Ruzic D N Temperature dependence of liquid-lithium sputtering from oblique 700 eV He ions 2003 *JNM* **313–16** 641–645

[39]   Wittmaack K 2001 Reliability of a popular simulation code for predicting sputtering yields of solids and ranges of low-energy ions *J. of App. Phys.* **96** 2632-7

[40]   Grossman A, Doerner R P and Luckhardt S 2001 Surface tension enhancement of TRIM sputtering yields for liquid metal targets *J. Nucl. Mat.* **290-293** 80-4

[41]   Krutenat R C and Panzera C 1970 Low-Energy Ar+ Sputtering Yields of Solid and Liquid Tin *J. of App. Physics* **41** 4953-7

[42]   Behrisch R and Eckstein W 2007 ed C E Ascheron *Sputtering by Particle Bombardment Experiments and Computer Calculations from Threshold to MeV Energies (Topics in Applied Physics)* Vol 110ISBN: 978-3-540-44502-9 (Berlin: Springer) p 509

[43]   Jorzick J, Loschm J, Kopnarski M and Oechsner H 2004 Detection in the ppm range and high-resolution depth profiling with the new SNMS instrument INA-X *Appl. Phys. A* **78** 655–8

[44]   Alcock C B, V P Itkin, and Horrigan M K 1984 Vapor pressure of the metallic elements *Canadian Metallurgical Quarterly* **23** 309

[45]   Coventry M D, Allain J P and Ruzic D N 2003 D+, He+ and H+ sputtering of solid and liquid phase tin J. Nucl. Mat. **313–316** 636–40

[46]   Hilborn R C 1982 Einstein coefficients, cross sections, f values, dipole moments, and all that *Am. J. Phys.* **50** 982–6

[47]   Sigmund P 1969 Theory of Sputtering. I. Sputtering Yield of Amorphous and Polycrystalline Targets *Phys. Rev.* **184** 383-416

[48]   Wehner G K 1956 Controlled Sputtering of Metals by Low-Energy Hg Ions *Phys. Rev.* **102 Nr. 3** 690-704

[49]   Mott N F and Massey H S W *The theory of atomic collisions* 1965(UK, Oxford University press) p 643

[50]   Teachout R R and Pack R T 1971 The static dipole polarizabilities of all the neutral atoms in their ground states *Atomic data* **3** 195-214

[51]   Fujimoto T and McWhirter R W P Validity criteria for local thermodynamic equilibrium in plasma spectroscopy *Phys. Rev. A* **42 Nr. 11** 6588-601

[52]   Hutchinson I H *Principles of plasma diagnostic* 2002 *2nd ed* (ISBN 0 521 80389 6, UK, Cambridge, Cambridge University press) p 226, 232, 240

[53]   Hajjar R J, Hollmann E M, Krasheninnikov S I and Doerner R P 2015 Modeling of aluminum impurity entrainment in the PISCES-A He+ plasma 2015 *JNM* **463** 664–667

[54]   Shumack A E, Schram D C , Biesheuvel J, Goedheer W J, and van Rooij G J 2011 Diagnosing ions and neutrals via n = 2 excited hydrogen atoms in plasmas with high electron density and low electron temperature *Phys. Rev. E* **83** 036402

[55]   Zielinski J J, van der Meiden H J, Morgan T W, 't Hoen M H J, Schram D C and De Temmerman G 2014 Self-shielding of a plasma-exposed surface during extreme transient heat loads *Appl. phys. letters* **104** 124102